New Organotin/CuCN/Quinazoline 3D-Supramolecular Coordination Polymers Having Catalytic and Luminescence Activities

Safaa Eldin H. Etaiw · Safaa N. Abdou

Abstract The new bimetallic supramolecular coordination polymers (SCP); $^3_\infty$[Cu(CN)$_2$·Me$_3$Sn·qaz], **1** and $^3_\infty$[Cu$_2$(CN)$_4$·(Ph$_3$Sn)$_2$·qaz], **2** (qaz = quinazoline), are prepared in water/acetonitrile solvent at room temperature. The structure of **1** consists of the anionic Cu(CN)$_2$ building blocks connected by the Me$_3$Sn cations to form zigzag chains which are bridged by qaz creating 2D-sheets. The interwoven infinite sheets are arranged in parallel A···A···A fashion developing 3D-network structure via H-bonds, π–π stacking, and Cu–C contacts. The network structure of **2** exhibits two different copper sites forming two Cu(CN)$_2$ building blocks which are connected by the Ph$_3$Sn groups constructing elongated corrugated chains. The qaz ligand connects these chains forming 3D-network structure containing the rhombic [Cu$_2$(μ$_3$-CN)$_2$] motif. **1** and **2** are luminescent materials which can be used in applications as molecular sensing systems. Also, the catalytic activity of **1** and **2** was investigated towards the degradation of Metanil Yellow (MY) dye by dilute solution of hydrogen peroxide as oxidant.

S. E. H. Etaiw (✉) · S. N. Abdou
Chemistry Department, Faculty of Science,
Tanta University, Tanta, Egypt
e-mail: safaaetaiw@hotmail.com

1 Introduction

The assembling of molecules to form stable multi dimensional aggregates is the quintessence of the self-recognition and self aggregation processes which are supramolecular chemistry paradigms. The understanding of the collective properties of the supramolecular compounds requires a profound knowledge of the interactions acting among molecules and ions in the solid state [1–3].

The combination of intra- and intermolecular bonding features of the ligands with variable valence state of copper (I) can be utilized to devise solids with predefined physical and chemical features such as nano-porous materials, gas storage, luminescence, biology and catalysis [4–9]. Strong and directional hydrogen bonding can also be exploited to fix the building blocks in rigid skeletons leaving channels and cavities [10–13].

The structural variability and flexibility of the R$_3$Sn organometallic systems as well as the effect of solvent on the formation of supramolecular organometallic solids were investigated to obtain materials exhibiting nano-porous structure and channels or cavities [14–20]. In continuing of our research work, the organometallic compounds; Me$_3$SnCl, (n-Bu)$_3$SnCl and Ph$_3$SnCl are used to be one of the ternary adducts in a simple reaction with K$_3$[Cu(CN)$_4$] and quinazoline (qaz) at room temperature. In the case of Me$_3$SnCl two products are obtained by changing the solvent from petroleum ether to acetonitrile producing [Cu$_2$(CN)$_2$·qaz]$_\infty$, **3** [21] and yellow prismatic crystals $^3_\infty$[Cu(CN)$_2$·Me$_3$Sn·qaz], **1**, respectively. SCP **3** is unexpectedly tin free orange needle crystals. On the other hand, in the case of (n-Bu)$_3$SnCl no product was obtained under the used experimental conditions. However, in the case of Ph$_3$SnCl, yellow crystalline product of $^3_\infty$[Cu$_2$(CN)$_4$·(Ph$_3$Sn)$_2$·qaz], **2** was formed with low quality crystals which are not suitable

for X-ray diffraction measurements. The qaz ligand as a planer molecule with extended delocalization π-system has been selected as potential donor instead of qox [18, 19] to investigate qaz complexing capability on the propagation of multi dimensional structures. The presence of the organotin fragment as well as qaz permits the formation of self inter-molecular hydrogen bonds which play a fundamental role in creating 3D-networks. The luminescence behavior and the catalytic activity of the SCP **1** and **2** are also investigated.

2 Experimental

2.1 Materials

All the reactions in this study were carried out using ternary adducts which are $K_3[Cu(CN)_4]$, organotin chloride and qaz. $K_3[Cu(CN)_4]$ was prepared following the literature procedure [22]. Organotin chlorides which are mainly, trimethyltin chloride and triphenyltin chloride as well as qaz were purchased from Aldrich, Sigma and Fluka and used without further purification. Acetonitrile was of analytical grade which was supplied by Aldrich and was used as received. Metanil Yellow (MY) (98% purity) was received from B.D.H. Chemicals Ltd and used as received.

2.2 Synthesis of $^3_\infty[Cu(CN)_2 \cdot Me_3Sn \cdot qaz]$, **1**

A solution of 90 mg (0.31 mmol) of $K_3[Cu(CN)_4]$ in 5 mL H_2O was added, with gentle stirring to a mixture of solutions containing 189 mg (0.95 mmol) of Me_3SnCl in 5 mL acetonitrile and 40 mg (0.31 mmol) of qaz, in 5 mL acetonitrile. Already, after some days, yellow prismatic crystals started growing from the initially clear solution. After filtration, washing with small quantities of cold H_2O and acetonitrile and overnight drying, 84 mg (67% referred to $K_3[Cu(CN)_4]$) of the yellow prismatic crystals of **1** were obtained. Elemental analysis data for $C_{13}H_{15}N_4CuSn$ are; Anal. Calc. C, 38.14; H, 3.67; N, 13.69; Cu, 15.54 and Found C, 38.20; H, 3.74; N, 13.61; Cu, 15.44.

2.3 Synthesis of $^3_\infty[Cu_2(CN)_4 \cdot (Ph_3Sn)_2 \cdot qaz]$, **2**

A solution of 90 mg (0.31 mmol) of $K_3[Cu(CN)_4]$ in 5 mL H_2O was added drop wise with gentle stirring to a solution of 366 mg (0.95 mmol) of Ph_3SnCl and 40 mg (0.31 mmol) of qaz, in 10 mL acetonitrile. A yellow precipitate was formed at once. After filtration, subsequent washing with H_2O and acetonitrile and overnight drying, about 305.7 mg (93% referred to $K_3[Cu(CN)_4]$) of yellow precipitate was obtained. All attempts to grow single crystals of **2** suitable for X-ray studies have so far ended up with the formation of microcrystalline powder with low quality crystals.

Elemental analysis data for $C_{48}H_{36}N_6Cu_2Sn_2$ are; Anal. Calc. C, 54.31; H, 3.39; N, 7.92; Cu, 11.98 and Found C, 54.48; H, 3.40; N, 7.87; Cu, 11.93.

2.4 Instruments

Microanalyses (C, H, N) were carried out with a Perkin-Elmer 2400 automatic elemental analyzer, while copper was determined using Perkin-Elmer 2380 atomic absorption spectrometer. Infrared (IR) spectra were recorded on a Bruker Vector 22 spectrophotometer as KBr discs, in the range of 4,000–400 cm^{-1}. ^1H and ^{13}C NMR spectra were recorded on a Bruker DPX 200 spectrometer, using DMSO-d_6 as a solvent. Mass spectra were recorded on a Finnigan MAT 8222 by FAB spectrometer. Thermogravimetric analyses were carried out on TGA–50H thermal analyzer (under N_2 atmosphere), in the range of 25–800 °C at a heating rate 20 °C/min. Electronic absorption spectra were measured on a Shimadzu (UV-3101 PC) spectrometer. A shaker water thermostat (Julabo SW20C) was used to shake the heterogeneous catalytic reaction mixture at 120 rpm at fixed temperature ±0.1 °C. Fluorescence spectra of solids were carried out using a Perkin-Elmer (LS 50 B) spectrometer at excitation wavelength 280 nm. X-ray powder diffraction patterns were recorded using a Diano Corporation diffractometer equipped with Co K$_\alpha$ radiation tube operated at 45 kV, 9 mA. X-ray Diffraction of single crystals was measured using the Kappa CCD Enraf–Nonius FR590 four circle goniometer with a graphite monochromatic Mo K$_\alpha$ radiation source ($\lambda = 0.71073$ Å) operated at 20 mA/50 kV.

2.5 X-Ray Crystallography and Structure Determination

The well developed crystal of **1** was mounted on glass fibers, and the measurements were made at 25 ± 2 °C. The structure was solved using direct-methods and all of the non-hydrogen atoms were located from the initial solution or from subsequent electron density difference maps during the initial stages of the refinement. After locating all of the non-hydrogen atoms in the structure, the model was refined against F^2, first using isotropic and finally anisotropic thermal displacement parameters. The positions of the hydrogen atoms were then calculated and refined isotropically, and a final cycle of refinements was performed.

2.6 Catalytic Activity Measurements

For the catalytic runs a stock solution of MY dye (4×10^{-5} M) was prepared in doubly distilled water. Hydrogen peroxide (30% V/V, Merck) was used. The initial concentration of H_2O_2 was determined with standard $KMnO_4$ solution. A number of reactors (100 mL) containing

a definite quantity of the catalyst (0.05 mmol) together with appropriate volume (3 mL) of MY dye solution (4×10^{-5} M) were placed in a water shaker thermostat at 25 °C to attain this temperature. To each reactor 1 mL of 0.5 M H_2O_2 solution was added and the time was noted. At regular time intervals, aliquot of each flask was withdrawn and the absorbance was recorded.

3 Results and Discussion

3.1 Crystal Structure of 1

The reaction of the ternary adducts $K_3[Cu(CN)_4]$, Me_3SnCl and qaz in water/acetonitrile solvent at room temperature, affords yellow prismatic crystals of the empirical composition $^{3}_{\infty}[Cu(CN)_2 \cdot Me_3Sn \cdot qaz] \equiv ^{3}_{\infty}[Cu(CN)_2 \cdot \mu\text{-}Me_3Sn \cdot \mu\text{-}qaz]$, **1**. The lattice constants, density and refinement parameters of **1** are collected in Table 1, while the inter-molecular bond lengths and bond angles are collected in Table 2. The ORTEP drawing of the asymmetric unit of **1** shows one copper atom, one Me_3Sn unit, two cyanide ligands and one qaz molecule, Fig. 1. The Cu(I) atom locates at an inversion center and adopts distorted TP-3 geometry via coordination to two ordered cyanide ligands and to N(22) atom of the qaz molecule. The angles of the TP-3 deviate than being 120° due to the close contacts between Cu(I) atom and C(26); Cu(2)–C(26) = 3.298 Å, the case which would adopt puckered zigzag chains containing the more acute angles, Table 2. The ordered cyanide groups assume, nearly linear configuration while the Cu–C distances are in the normal reported range [23–32]. On the other hand, the Cu(2)–N(22) distance is notably in most cases, shorter than those observed in the prototype polymers [14, 15, 22–25, 28, 33–36]. The Cu(CN)$_2$ fragments represent the main building blocks of the structure of **1** which are bridged by the Me_3Sn^+ cations to construct 1D-infinite parallel zigzag chains along the *c*-axis, Fig. 2. The tin atom is coordinated to thee methyl groups and two nitrogen ends of the two cyanide ligands in axial positions via coordinate bonds forming TBPY-5 geometry. The methyl groups of the tin atoms turn out to have high thermal parameters due to rapid mobility of the methyl ligands. The occupancy of the carbon and hydrogen atoms of the methyl group are 0.5 while that of C(35) is 1 exhibiting the highest value of thermal parameter. This unique behavior of the Me_3Sn fragment is crystallographically supported by the presence of two sets of angles of the TP-3 geometry around the tin site being close to 120°; Table 2. The rotation of the methyl groups of the Me_3Sn fragment is previously supported by the ^{13}C and ^{119}Sn solid state NMR spectra of $[Co(CN)_4(CNSnMe_3OH_2)_2]^-$ anion, **4** [37], $[(^nBu_4N)(Me_3Sn)Cu_2(CN)_4]$, **5** [17] and Me_3SnCN, **6**

[17, 38]. In the ^{13}C NMR spectrum of **4** two sets of methyl carbon atoms give rise to two equally intense singlets at $\delta(C) = 1.2$ and 2.2 ppm accompanied by weak satellite doublets due to the presence of ^{117}Sn and ^{119}Sn nuclei. The appearance of just two $^{13}C(Me)$ signals at room temperature, in spite of the existence of six crystallographically non-equivalent methyl carbon atoms, is explained by rapid rotation of the two different Me_3Sn groups about their N–Sn–O axes [37]. On the other hand, the ^{13}C CPMAS spectrum of **5** clearly showed the existence of a single type of the methyl groups for the Me_3Sn unit, presumably because of motional averaging, at $\delta(C) = 0.7$ ppm with tin satellites. In addition, the appearance of only one ^{119}Sn centre band, one methyl ^{13}C signal ($\delta(C)$ −1.1 ppm) and one cyanide carbon 2:1 doublet for neat Me_3SnCN supports the view that there are regular {–Sn–CN–Sn–CN–} chains with rapidly rotating Me_3Sn units in this compound [17, 38].
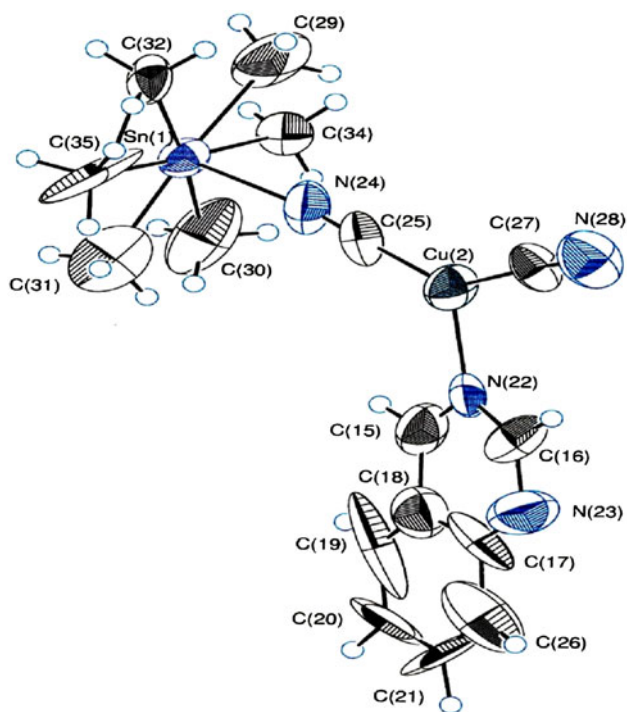
The two Sn(1)–N(24) and Sn(1)–N(28) distances of 2.289(6) and 2.386(2) Å, respectively, are common for polymers built up of {–M–CN–Sn–NC–} chains [15, 17], as are the slightly reduced (from 180°) C–N–Sn angles, Table 2. The N(24)–Sn(1)–N(28) angle; 179.30°, is linear exhibiting similar structure as that present in [CuCN· Me_3SnCN·pyz] [15]. The relatively bent structures of the

Table 1 Crystal data and structure refinement parameters of $^{3}_{\infty}[Cu(CN)_2 \cdot Me_3Sn \cdot qaz]$, **1**

Empirical formula	$C_{13}H_{15}N_4CuSn$
Formula weight (g mol^{-1})	409.527
Temperature (K)	298
Wavelength (Å)	0.71073
Crystal system	Monoclinic
Space group	$P2_1/c$
Unit cell dimensions	
a (Å)	11.6055 (4)
b (Å)	11.1671 (6)
c (Å)	14.1182 (9)
α (°)	90.00
β (°)	120 (18)
γ (°)	90.00
V (Å^3); Z	1596.45 (15)/4
$D_{calc.}$ (g cm^{-3})	1.704
F (000)	692
Θ-range (°)	2.910–27.485
Reflections collected/unique	11748/1138
R_{int}	0.062
Data/restraints/parameters	1138/0/194
R indices [$I > 3\sigma(I)$] R_1/wR_2	0.070/0.146
$W = 1/s^2$ (Fo^2) + $0.10000 \times$ Fo^2)	
R indices (all data)	0.253/0.184
Largest difference peak and hole (e Å^{-3})	2.67/−3.91

Table 2 Selected bond lengths (Å) and bond angles (°) for **1**

Sn(1)–N(24)	2.289(6)	N(24)–Sn(1)–C(35)	89.0(2)
Sn(1)–N(28)	2.386(2)	N(24)–Sn(1)–N(28)	179.30
Sn(1)–C(30)	2.13(2)	C(30)–Sn(1)–C(32)	174.6(6)
Sn(1)–C(32)	2.197(12)	C(30)–Sn(1)–C(29)	116.8(8)
Sn(1)–C(29)	2.18(2)	C(30)–Sn(1)–C(29)	116.8(8)
Sn(1)–C(31)	2.14(2)	C(30)–Sn(1)–C(35)	122.5(6)
Sn(1)–C(34)	2.302(12)	C(32)–Sn(1)–C(31)	112.6(6)
Sn(1)–C(35)	2.14(2)	C(32)–Sn(1)–C(34)	124.1(5)
Cu(2)–N(22)	2.066(6)	C(29)–Sn(1)–C(35)	120.7(6)
Cu(2)–C(25)	1.893(7)	C(31)–Sn(1)–C(34)	123.3(5)
Cu(2)–C(27)	1.868(6)	N(22)–Cu(2)–C(25)	113.0(3)
C(27)–N(28)	1.120(7)	N(22)–Cu(2)–C(27)	107.4(3)
C(25)–N(24)	1.158(7)	C(25)–Cu(2)–C(27)	139.6(3)
Cu(2)–C(27)–N(28)	175.1(7)	Cu(2)–N(22)–C(16)	117.6(5)
N(24)–Sn(1)–C(30)	90.9(4)	Cu(2)–N(22)–C(15)	126.4(6)
N(24)–Sn(1)–C(32)	92.8(4)	Cu(2)–C(25)–N(24)	178.7(7)
N(24)–Sn(1)–C(29)	86.7(5)	Sn(1)–N(24)–C(25)	171.9(6)
N(24)–Sn(1)–C(31)	87.3(4)	Sn(1)–N(28)–C(27)	173.07
N(24)–Sn(1)–C(34)	91.4(3)	–	–

Fig. 2 A view of the 2D-sheet of the SCP **1** down the projection of *c*-axis showing the 1D-infinite parallel zigzag chains connected by H-bonds

Fig. 1 Perspective view of the asymmetric unit of the SCP **1**, showing the atom labeling scheme and thermal *ellipsoids* are shown 50% probability

C–N–Sn and Cu–C–N angles, compared with those present in the prototype polymers [14–17, 39], may be considered as indicative of a rational design to avoid substantial steric constraints. Surprisingly, there are extensive H-bonds in

the chain; 2.439–3.097 Å, due to the presence of the methyl groups and the qaz ligand, S. 1. The 1D-{–Cu–CN–Sn–NC–Cu–} zigzag chains are bridged by unique H-bonding formed between C(27)–H(21) = 2.872 Å, C(20)–H(29B) = 3.010 Å and C(29)–H(20) = 3.093 Å creating 2D-sheets down the projection of the *c*-axis, Fig. 2. In this case, qaz molecule bridges the chains through the Cu(I) atom in one chain via N(22) and through H-bonds with C(27) of the cyanide group and C(29) of the methyl group in another chain. Such unprecedented bridging capability of the qaz ligand creates the distorted 18-atom hexagonal ring structure, [$Sn_2Cu_3C_5N_4(N_2H_2)_{qaz}$] in the ab-plane with the dimensions of 12.932 Å × 16.321 Å, Fig. 2. The sheets are further stabilized by π–π stacking; 3.045–3.338 Å. This structure represents yet another variant of the honeycomb net observed previously in a number of prototype compounds [23, 26–29, 32, 34–36, 40–43]. The wide space in the fused hexagonal rings in the 2D-sheet, along the *a*-axis, has the capability to accommodate the qaz and the Me ligands where the mobile methyl groups rotate freely like a fan in the space of the ring, Fig. 3. Alternatively, the infinite sheets arranged in parallel A···A···A fashion, down the projection of the *b*-axis, while the methyl groups look like pillars between the sheets, Fig. 4a. On the other hand, along the *a*- or the *c*-axes they are interwoven developing 3D-network structure, Fig. 4b. There are different interlayer distances due to interweaving of the sheets where the shortest distances are in the range of 2.377–6.576 Å. Close packing effects via extensive H-bonds; 2.377–3.004 Å, π–π stacking; 3.416–3.695 Å, Cu–C contacts; Cu(2)–C(26) = 3.298 Å, Cu(2)–N(22) = 3.417 Å and Van der Waals; 3.714 Å cause stabilization of the 3D-network structure of **1**, S. 2. Most H-bonds are between methyl groups in the neighboring sheets where the methyl groups are interfering with each others.

It is worth mentioned that, the crystal structure of **1** contains the qaz molecule not as a guest molecule but rather as a ligand coordinated to the Cu(I) atom. The encapsulation of uncharged or ionic guests (i.e. templates) into the cavities of the CuCN SCP containing (R₃Sn) fragments has attracted much interest in order to reduce or even to fully exclude, lattice interpenetration. Examples of such frameworks hosting only one, sterically appropriate, guest component range from KH_2PO_4 [44] to e.g. [Cd$(CN)_2 \cdot CMe_4$] [45], [(NMe₄)Cu^{I}Zn^{II}(CN)₄] [17], [Ph₃Sn)₂Ni$(CN)_4 \cdot Ph_3SnOH$] [46], [(^{n}Bu₄N)(Et₃Sn)₂Cu(CN)₄] [17] and [(^{n}Bu₄N)(Me₃Sn)Cu₂(CN)₄] [39]. In some cases, the organic free [(Me₃Sn)₃Cu(CN)₄] or [(Me₃Sn)₂Cu₂(CN)₄] [47] complexes are obtained while in other cases the desired (Sn/Cu) stoichiometric ratio would not obtained. The reaction of Me₃SnCl and K₂[Zn(CN)₄] (2:1) in aqueous solution or liquid NH₃ affords a precipitate of unforeseen composition [(Me₃Sn)Zn(CN)₃] instead of the [(Me₃Sn)₂Zn(CN)₄] which was not obtained [17]. The (Sn/Cu) stoichiometric ratio in **1** is 1:1 which is surprisingly avoid any one of the expected ratios of 2:1, 1:2, 2:2 or even 3: 3 [17, 39]. Surprisingly, the prototype SCP containing qox molecule instead of qaz, using the same adducts and the reaction conditions, exhibit 1: 2 and 2: 2 (Sn/Cu) ratios, [Cu₂(CN)₃·Me₃Sn·qox] and [Cu₂(CN)₄·(Ph₃Sn)₂·qox] while in the case of Bu₃SnCl, the tin free product, [Cu₂(CN)₂·qox] was obtained [21].

Comparing the crystal structure of **1** with that of the formal congeners of $\infty^3[\{Cu_2(CN)_3\}\mu\text{-}(Me_3Sn)\mu\text{-}(qox)]$, **7** [19] indicates the formation of [–Cu–CN–Me₃Sn–NC–Cu–] corrugated chains connected by qox forming 2D-layers containing distorted hexagonal rings. The Cu(I) atoms assume TP-3 geometry while the tin atom exhibits TBPY-5
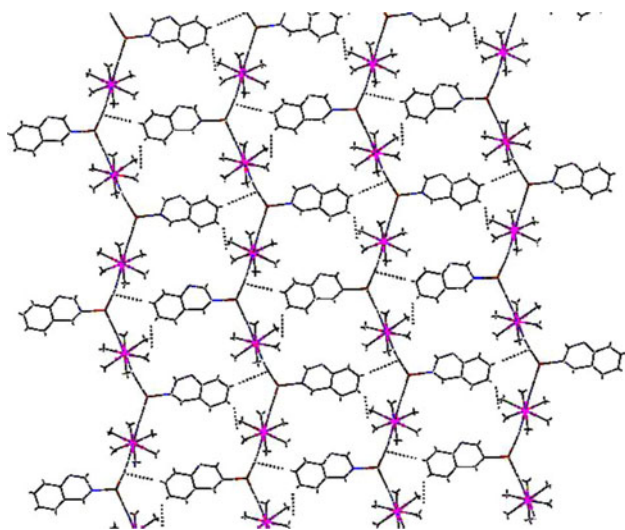
Fig. 3 Visualization of the 2D-sheet of the SCP **1** down the projection of the *a*-axis showing the mobile methyl groups rotating like a fan in the space of the network. H-bonds are represented by *dashed lines*
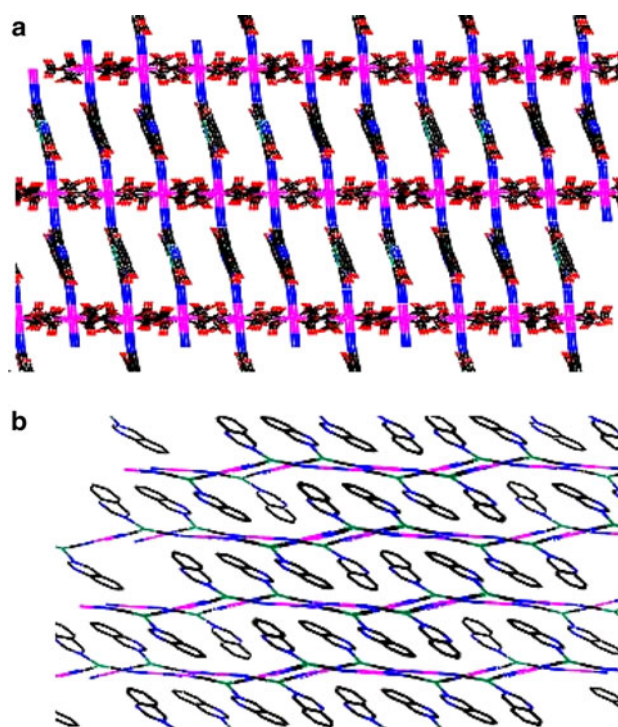
Fig. 4 a Visualization of the 3D-network structure of the SCP **1** down the projection of *b*-axis showing the methyl groups located in the space between the layers. **b** A view of the interwoven 2D-sheets of the SCP **1** in the ab-plane developing 3D-network structure. H atoms and methyl groups are omitted for clarity

configuration. The 3D-network of **7** is close packed by H-bonds and π–π stacking via interwoven of the layers. Obviously, the layers adopt non-interpenetrating open 3D-framework capable to accommodate the voluminous qox ligand and the methyl groups. However, the main differences between the structure of **1** and that of **7** are the A···A···A pattern structure present in **1** rather than the AB···AB···AB pattern present in **7** as well as the fact that copper(I) atoms in **1** avoid any interaction as the shortest distance between two copper(I) atoms is 4.258 Å while cuprophilic interaction is obvious in **7** ≈ 3.125 Å. However, the crystal structure of **1** is completely different than that of **7** as also indicated by the diffractograms of XRPD patterns calculated from the X-ray single crystal data. The crystal structure of **7** contains the anionic [Cu₂(CN)₃]⁻ building blocks while that of **1** consists of anionic [Cu(CN)₂]⁻ building blocks. On the other hand, the Sn/Cu ratio in **7** is 1:2 while in **1** is 1:1. In addition, qox molecule acts as μ₂-bridging ligand via the nitrogen atoms while qaz acts as μ₃-bridging ligand via one nitrogen atom and two hydrogen bonds with the C(27) and C(29) atoms. Although, the SCP$_\infty^3$[Cu₂(CN)₄(Ph₃Sn)₂·qox], **8** [18] crystallizes from the same ternary adducts used for the formation of **7** only by replacing the methyl groups by phenyl groups,

i.e. (Ph₃Sn), the crystal structure consists of super diamondoid 3D-lattice containing four minicycle [Cu₂(µ₃-CN)₂] motifs. The structure comprises also, surprisingly, non-interpenetrating 3D-network. The formulation of such super-diamondoid lattice should adopt instead a more compact, structure with, nevertheless, tetrahedral Cu atoms and bifurcated cyanide ligands to be capable of accommodating the more bulky phenyl ligands. Obviously, the size and the shape of the ligand (R) as well as of the bipodal ligand, play an essential role for verification and the actual structure of the envisaged non-interpenetrating systems [Cu$_n$(CN)$_m$·(R₃M)$_x$·L] where R = Me or Ph and L = qox or qaz ligand.

3.2 Infrared Spectra of **1** and **2**

The IR spectra of **1** and **2** exhibit the characteristic bands of the ternary adducts R₃Sn units, cyanide groups and qaz, S. 3 and S. 4. The stretching vibrations of the Sn–C bond exhibit a sharp strong band at 554 cm^{-1} which reflects the presence of the TBPY-5 configured Me₃SnN₂ connecting units in the network structure of **1** [17]. The presence of the cyanide ligand is indicated by the strong bands located at 2117 cm^{-1} ($\nu_{C\equiv N}$) and at 436 cm^{-1} (ν_{Cu-C}). The band at 2,117 cm^{-1} can be considered as a good evidence of the formation of non-linear chains of the [–Cu–C≡N–Me₃Sn–N ≡ C–Cu–] fragment [17, 47]. This opinion is further supported by the appearance of the medium band due to the stretching vibrations of the Cu–C bond as a single band at 436 cm^{-1}. So, the structure of **1** contains one type of the cyanide groups which is coordinated to one copper atom and one tin atom. On the other hand, the IR spectrum of **2** displays two bands at 2,112 and 2,081 cm^{-1} similar to those observed in the IR spectrum of **8** [18]. It might be speculated that **2** and **8** are isostructural as indicated by X-ray diffraction (vide infra). This is also substantiated by the presence of the bands at 550 and 563 cm^{-1} due to ν_{Sn-C} and the bands at 411 and 405 cm^{-1} due to ν_{Cu-C}, S. 4. Thus, in the structure of **2**, there are two different kinds of the cyanide ligands. The presence of qaz, in the network structure of **1** and **2** is supported by the bands due to ν_{CH}, $\nu_{C=N}$, $\nu_{C=C}$, δ_{CH}, ν_{C-N} and γ_{CH}, S. 3 and S. 4. Also, the overtone and combination bands of the phenyl rings appear as weak bands in the region of 1,990–1,716 cm^{-1}.

3.3 ¹H-NMR Spectra of **1** and **2**

The ¹H-NMR spectra of **1** and **2** show two important singlet peaks at 9.60 and 9.28 ppm corresponding to the protons H(4) and H(2) of the CH = N moiety, while the aromatic protons of qaz ligand give rise to one doublet at 8.13–8.18 ppm and two broad multiplets at 7.93–8.02 and 7.75–7.80 ppm. These peaks can be attributed to absorption of the protons; H(8), H(5,7) and H(6), respectively. This

assignment was supported by consulting the ¹H-NMR spectrum of qaz, which exhibits two sharp singlets, one doublet and two multiplets at 9.58, 9.27, 8.10–8.14, 7.97–8.00 and 7.73–7.77 ppm corresponding to H(4), H(2), H(8), H(5,7) and H(6), respectively. It is observed that the peaks of qaz in **1** and **2** are generally slightly shifted to downfield relative to those of qaz indicating the participation of qaz in the formation of the coordination sphere of copper. The broad multiplet at 7.75–7.80 ppm, in the NMR spectrum of **2**, is coincident with the peaks of Ph₃Sn protons. This assignment was substantiated by consulting the ¹H-NMR spectrum of Ph₃SnCl. The aromatic protons of the Ph₃Sn units give rise to absorption indicated by the two broad multiplet peaks at 7.44 and 7.77 ppm [48]. The peaks of the Ph₃Sn units in the spectrum of **2** suffer upfield shift relative to those of Ph₃SnCl supporting participation of the Ph₃Sn fragments in the structure of **2** as connecting units forming TBPY-5 configuration. Also, the ¹H-NMR spectrum of **1** shows one singlet peak for the Me₃Sn protons at 0.49 ppm which exhibits two satellite peaks that arise from the coupling to ¹¹⁷Sn and ¹¹⁹Sn nuclei [37, 47, 48]. The presence of these satellite peaks are good indication for the presence of Me₃Sn connecting units exhibiting TBPY-5 configuration.

3.4 ¹³C-NMR Spectrum of **2**

The ¹³C-NMR spectrum of **2** shows three multiplets at 128.69–130.29, 135.51–137.68 and 140.76–140.99 ppm and two sharp singlets with weak intensity at 155.95 and 161.60 ppm. Inspection of the ¹³C-NMR spectrum of **2** indicates the presence of the signals corresponding to the Ph₃Sn, qaz and cyanide ligands. The Ph₃Sn fragment absorbs at 129.28, 129.93 and 136.86 ppm [18] which appear in the first and the second multiplets at more or less the same position at 129.20, 129.67 and 136.95 ppm in the spectrum of **2**. The last signal at 136.95 ppm is accompanied by weak satellite doublets at 136.50 and 137.37 ppm due to the presence of ¹¹⁷Sn and ¹¹⁹Sn nuclei. On the other hand, the ¹³C-NMR spectrum of qaz itself displays strong sharp signals at 128.52, 128.66, 128.97, 135.43, 155.92 and 161.54 ppm in addition to two relatively weak signals at 125.55 and 150.11 ppm. These sharp signals corresponded to C(5), C(6), C(8), C(7), C(4), C(2), C(10) and C(9) respectively. These strong sharp signals appear as weak ones in the ¹³C-NMR spectrum of **2** at 128.69, 130.29, 135.51, 137.68, 155.95 and 161.60 ppm, respectively, while the weak signals at 125.55 and 150.11 ppm in the spectrum of qaz do not appear in the ¹³C-NMR spectrum of **2** under the used experimental conditions. The cyanide region has three signals at 140.76, 140.90 and 140.99 ppm, probably due, in part, to second order effects arising from dipolar coupling to the quadrupolar ¹⁴N nucleus [49]. Also, the multiplet centered at 129.67 ppm shows a signal at

129.86 ppm corresponding to another type of the cyanide ligand rather than those observed in the region of 140.76–140.99 ppm. Thus, the presence of two different regions due to the cyanide ligands indicates the presence of two types of the cyanide ligand in the structure of **2**.

3.5 Mass Spectra of 1 and 2

The FAB$^+$ mass spectra of **1** and **2** exhibit the base peaks at m/z 165 and 909 corresponding to Me$_3$Sn$^+$ and [Cu$_2$(CN)$_3$(Ph$_3$Sn)$_2$]$^+$ of the molecular ions, respectively. The mass spectra exhibit the ion peaks corresponding to the fragment ions of qaz and R$_3$Sn–NC–Cu fragments, Tables 3 and 4. The fragmentation mechanism of [qaz]$^+$ ion is illustrated in Scheme 1. Moreover, the peak of [Cu(CN)$_2$Me$_3$Sn(qaz)]$^+$ ion at m/z 410 is observed in the mass spectrum of **1** confirming the expected (M.W.). On the other hand, the mass spectrum of **2** shows the ion peaks at m/z = 120, 154, 197, 274, 351 and 377 which can be attributed to the presence of Sn$^+$, (C$_6$H$_5$)$_2^+$, PhSn$^+$, Ph$_2$Sn$^+$, Ph$_3$Sn$^+$ and Ph$_3$SnCN$^+$ fragments, respectively confirming the presence of the Ph$_3$Sn$^+$ connecting units in the structure of **2**. Also, the peak of [Cu$_2$(CN)$_4$(Ph$_3$Sn)$_2$(qaz)]$^+$ ion at m/z 1064 is observed confirming the expected (M.W.) of **2** which can be considered as a further support of the structure suggested by elemental analysis data.

The FAB$^-$ mass spectra of **1** and **2** display six and ten peaks of [Cu$_n$(CN)$_{n+1}$]$^-$ units, respectively, Tables 3 and 4. The base peak of **1** is observed at m/z 115 corresponding to [Cu(CN)$_2$]$^-$ of the molecular ion while that of **2** is observed at m/z 204 corresponding to [Cu$_2$(CN)$_3$]$^-$ of the molecular ion. Thus, the mass spectra of **1** and **2** confirm the presence of qaz, R$_3$Sn and CuCN units in their structures and support the polymeric nature of the Cu$_n$(CN)$_m$ building blocks. It is worth mentioned that the mass spectra of **2** is quite similar

Table 3 The data of the positive and negative ion FAB mass spectra of $^3_\infty$[Cu(CN)$_2$·Me$_3$Sn·qaz], **1**

Assignment	m/z	Assignment	m/z
C$_4$H$_2^+$	50	Me$_3$SnCN$^+$	191
C$_6$H$_4^+$	76	[qaz-CuCN]$^+$	220
C$_7$H$_5$N$^+$	103	[Cu(CN)$_2$MeSn]$^+$	250
Sn$^+$	120	[CuCNMe$_3$Sn]$^+$	255
[qaz]$^+$	130	[Cu(CN)$_2$Me$_3$Sn]$^+$	283
MeSn$^+$	135	[CuCNMe$_3$Sn(qaz)]$^+$	384
Me$_2$Sn$^+$	150	[Cu(CN)$_2$Me$_3$Sn(qaz)]$^+$ ≡ [M]$^+$	410
Me$_3$Sn$^+$	165	[Cu$_2$CNMe$_2$Sn(qaz)]$^+$	433
Me$_2$SnCN$^+$	176	[Cu$_2$(CN)$_4$(MeSn)$_2$]$^+$	449
[Cu(CN)$_2$]$^-$	115	[Cu$_4$(CN)$_5$]$^-$	384
[Cu$_2$(CN)$_3$]$^-$	204	[Cu$_5$(CN)$_6$]$^-$	474
[Cu$_3$(CN)$_4$]$^-$	295	[Cu$_6$(CN)$_7$]$^-$	563

Table 4 The data of the positive and negative ion FAB mass spectra of $^3_\infty$[Cu$_2$(CN)$_4$·(Ph$_3$Sn)$_2$·qaz], **2**

Assignment	m/z	Assignment	m/z
C$_4$H$_2^+$	50	[Cu$_2$(CN)$_2$Ph$_2$Sn(qaz)]$^+$	583
C$_6$H$_4^+$	76		
C$_7$H$_5$N$^+$	103		
Sn$^+$	120		
[qaz]$^+$	130	[Cu$_2$CNPh$_3$Sn(qaz)]$^+$	636
(C$_6$H$_5$)$_2^+$	154		
[Cu-qaz]$^+$	194	[Cu$_2$(CN)$_2$Ph$_2$Sn(qaz)PhSn]$^+$	779
PhSn$^+$	197	[Cu$_2$(CN)$_3$(Ph$_3$Sn)$_2$]$^+$	909
Ph$_2$Sn$^+$	274	[Cu$_2$(CN)$_2$(Ph$_3$Sn)$_2$(qaz)]$^+$	1,014
Ph$_3$Sn$^+$	351	[Cu$_2$(CN)$_4$(Ph$_3$Sn)$_2$(qaz)]$^+$ ≡ [M]$^+$	1064
Ph$_3$SnCN$^+$	377	[Cu$_2$(CN)$_4$(Ph$_3$Sn)$_2$(qaz)Ph$_2$Sn]$^+$	1,336
[Cu(CN)$_2$]$^-$	115	[Cu$_6$(CN)$_7$]$^-$	564
[Cu$_2$(CN)$_3$]$^-$	204	[Cu$_7$(CN)$_8$]$^-$	652
[Cu$_3$(CN)$_4$]$^-$	295	[Cu$_8$(CN)$_9$]$^-$	741
[Cu$_4$(CN)$_5$]$^-$	384	[Cu$_9$(CN)$_{10}$]$^-$	831
[Cu$_5$(CN)$_6$]$^-$	474	[Cu$_{10}$(CN)$_{11}$]$^-$	921
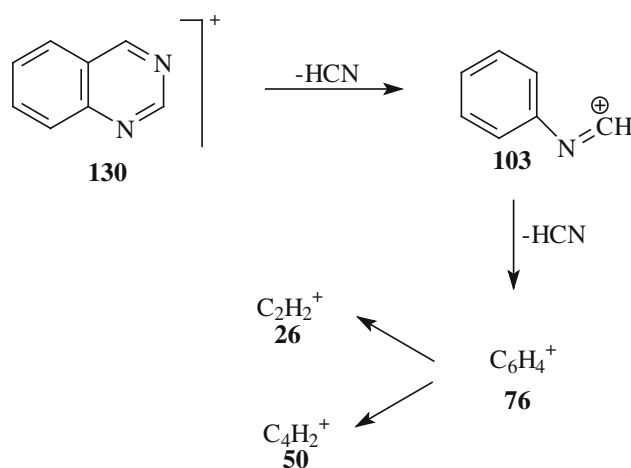
Scheme 1 Fragmentation of [qaz]$^+$ ion.

to those of $^3_\infty$[Cu$_2$(CN)$_4$·(Ph$_3$Sn)$_2$·qox], **8**, S. 5 and S. 6, indicating that they contain the same fragments and that **2** is isostructure to **8** (vide infra) [18].

3.6 Thermogravimetric Analyses of 1 and 2

The SCP **1** undergoes thermolysis in four steps, S. 7. The first step is in the temperature range 110–200 °C and it is due to the decomposition of the more volatile connecting unit Me$_3$Sn. This step is followed by the loss of qaz molecule in the temperature range 220–350 °C. The third step corresponds to the loss of two cyanide groups in the temperature range 365–500 °C. Over 550 °C, complete decomposition occurs producing copper, S. 7. Also, the SCP **2** undergoes thermolysis in four steps. The first step takes

place in the temperature range 100–230 °C and it corresponds to releasing of one qaz molecule. This step is followed by the loss of one unit of Ph$_3$Sn in addition to the release of four cyanide groups in the temperature range 235–290 °C. The third step between 295 and 420 °C, is due to the removal of the three phenyl groups of the other Ph$_3$Sn unit. In the temperature range 420–450 °C, the residue was found to be the mixed metals, Sn + 2Cu. In the temperature range 455–550 °C, the mass increases due to the gain of the mass of an oxygen atom [observed $\Delta m = +1.52\%$ (16.2 g mol^{-1}), calculated $\Delta m = +1.50\%$ (16 g mol^{-1})]. At higher temperatures over than 600 °C, tin suffers oxidation leading to the product of SnO$_2$. The molecular weight of the residue obtained after complete thermolysis of **2** is coincident with 0.5Sn + 0.5(SnO$_2$) + 2Cu [observed mass = 24.9% (264.06 g mol^{-1}), calculated mass = 24.68% (261.8 g mol^{-1})], S. 7. It is worth mentioned that the thermogravimetric data of **2** are quite similar to those of **8** [18] indicating that the SCP **2** has the same thermolysis mechanism and the same structure of **8**.

3.7 X-Ray Powder Diffraction and the Structure of 2

Spectroscopic data as well as elemental and thermal analyses show that **2** has the chemical formula $^3_\infty$[Cu$_2$(CN)$_4$·(Ph$_3$Sn)$_2$·qaz] which is the same as that of **8**, $^3_\infty$[Cu$_2$(CN)$_4$·(Ph$_3$Sn)$_2$·qox]. The experimental X-ray powder diffractograms of **2** and **8** have the same reflections, 2θ values and the lattice constants, Fig. 5, indicating that they are isostructural. Thus, the network structure of **2** exhibits two crystallographically different copper sites forming two Cu(CN)$_2$ building blocks which are connected by the Ph$_3$Sn groups constructing elongated corrugated chains. The qaz ligand connects these chains forming 3D-network structure containing the rhombic [Cu$_2$(μ$_3$-CN)$_2$] motif as gathered from the ^{13}C-NMR spectrum of **2** which exhibits two different peaks corresponding to two different kinds of the cyanide group. The tin sites are coordinated to three phenyl groups and two cyanide ligands in axial positions via coordinate bonds forming TBPY-5 configuration. The network structure of **2** can be considered as consisting of repeating units of the unique rhombic [Cu$_2$(μ$_3$-CN)$_2$] motif connected by the CN–Sn–NC spacer on one side and by the qaz spacer on the other side forming 3D-network. In this case, three different kinds of rings are formed. The 3D-network structure of **2** acquires non-interpenetrating rings creating box-like structure with cavities suitable to accommodate the bulky phenyl groups.

3.8 Electronic Absorption and Emission Spectra of 1 and 2

The electronic absorption spectra of qaz, **1** and **2** display three absorption bands at 220–225, 270–275 and
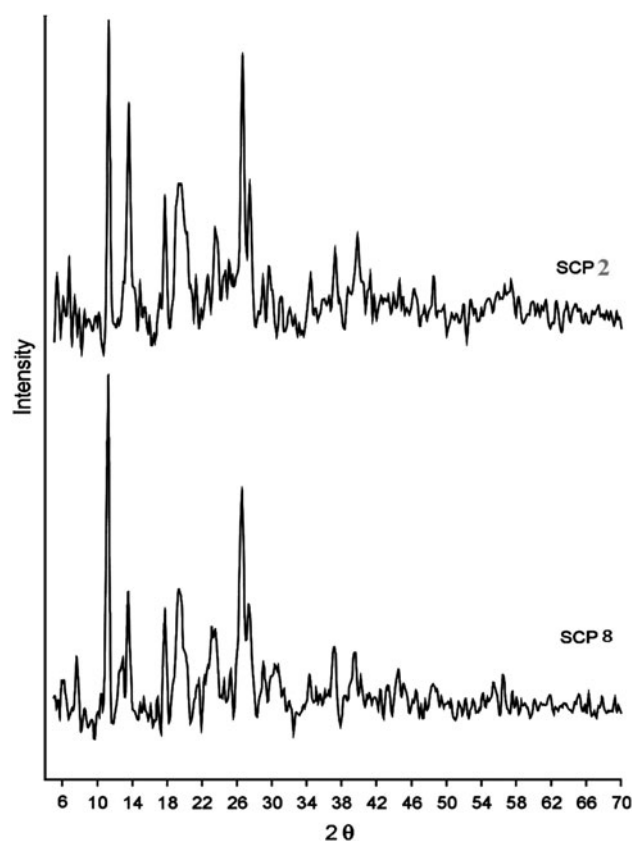

Fig. 5 X-ray powder diffraction of the SCP **2** and **8**

300–310 nm. The spectrum of qaz resembles that of naphthalene [50]. These bands correspond to ^{1}B$_b$ ← ^{1}A, ^{1}L$_a$ ← ^{1}A and ^{1}L$_b$ ← ^{1}A, respectively [50]. These bands appear at more or less the same wavelengths in the electronic absorption spectra of **1** and **2**, Table 5. However, the band at 310 nm in the spectrum of qaz exhibits blue shift in the spectra of **1** and **2** due to coordination of qaz to the copper atom. The emission spectrum of qaz displays one broad symmetrical band at 450 nm corresponding to the lowest π–π* state in qaz. On the other hand, the emission spectra of **1** and **2** display three bands centered at 385–390, 418–430 and 475 nm, Table 5. The emission band of qaz suffers a shift to higher energy in the emission spectra of **1** (430 nm) and **2** (418 nm) under the effect of coordination of qaz to the copper site. On the other hand, the possible photophysical sources of luminescence behavior in **1** and **2**, for the remaining two peaks at 390 and 475 nm, can be argued to the MC transition and MLCT, respectively. The emission band at 385 nm of **1** and that at 390 nm of **2** resembles that of CuCN [51] which is assumed to arise from transitions from the lowest excited-triplet state to the ground state. Lifetime studies of soluble Cu(1)-cyano species have suggested that emission is usually a phosphorescence phenomenon [52, 53].

Table 5 The electronic absorption and emission spectra of **1** and **2**

| λ_{abs} (nm)				λ_{em} (nm)			
Qaz	**1**	**2**	Assignment	Qaz	**1**	**2**	Assignment
220	220	225	$^1B_b \leftarrow {}^1A$	–	385	390	MC
270	275	270	$^1L_a \leftarrow {}^1A$	450	430	418	Lowest π–π^* State
310	300	300	$^1L_b \leftarrow {}^1A$	–	475	475	MLCT

3.9 Catalytic Studies

The presence of dyes in water effluents is a problem of great environmental concern. Concerning environment protection, hydrogen peroxide is a desirable oxidant but its activation to generate an efficient oxidant species is still a challenge. Addition of catalyst leads to activate the generation of HO˙ (which is the oxidant species) [54–57]. The catalytic oxidation of MY dye was studied using H_2O_2 as oxidant and the SCP **1** or **2** as heterogeneous catalysts. When MY dye was added to hydrogen peroxide in the absence of any one of the SCP **1** or **2** catalyst no changes in the absorption spectrum have been observed indicating that H_2O_2 alone is unable to degrade the MY dye. The reaction was initiated when any one of the SCP **1** or **2** was added as catalyst. Thus, when the SCP catalyst **1** or **2** was added, a reaction occurred leading to a color removal of the dye, Fig. 6. The final solution is completely bleached after 3–3.5 h as illustrated by the absorption spectra of MY in water (at $\lambda_{max} = 435$ nm) at the beginning and end of the reaction, Fig. 6. The catalytic activity of **1** is more pronounced than that of **2** since the ratio of degradation decreases on going from **1** to **2**. After 60 min, there is a fast degradation of the MY dye. On the other hand, after 2 h about 83% of the MY dye is degraded in the case of catalyst **1** while for **2** about 68% of MY dye is degraded. This means that the two SCP **1** and **2** have catalytic activity towards the degradation of MY dye. An important issue that must be addressed while studying liquid-phase oxidations over a solid catalyst is a possibility of catalyst recycling. In each case, after the end of the first experiment, the catalyst is washed with double distilled water, dried, and then starting a new experiment. It was found that the SCP **1** and **2** maintained their catalytic activity for two cycles of the dye oxidation with hydrogen peroxide. It is worth mentioned that the components of these SCP (K3[Cu (CN)4], organotin chloride and the organic ligands) have no catalytic activity towards the degradation of MY dye when they are tested at the same conditions. On the other hand, investigation of the catalysts after the catalytic cycle by elemental analysis and the IR spectra, Fig. 7, show that the catalysts are stable keeping their identity. Also, magnetic susceptibility measurements reveal that the used catalysts are still diamagnetic which indicates that the

structures of the SCP catalysts **1** and **2** after the catalytic cycles remain containing the Cu(I)CN building blocks. Further study concerning the mechanism and the factors affecting the reaction rate is currently carried out.

4 Conclusion

The present procedure of syntheses of **1** and **2** at room temperature, in spite of being surprisingly simple, affords the formation of precipitates of **1** and **2** which are consisting exclusively of one discrete species and never of any mixture of different assemblies. It should also be pointed out that, until recently no cyanide bridged bimetallic complexes have been reported by the solvothermal technique. The SCP **1**, **2**, **7** and **8** exhibit variable stoichiometries in spite of the fact that the reactions were mostly performed using equimolar ratios for the reactants in all cases. It seems that self assembly of either authentic or in situ prepared $K_3[Cu(CN)_4]$, R_3SnCl and bipodal ligand takes place at the appropriate stoichiometry required by the extended framework structure to adopt enough space demanded by the R_3Sn fragment and the bipodal bridging ligand. The cyanide ligand proves its versatility as bridging ligand. It exhibits μ_2 or μ_3 bridging capability producing the rhombic $[Cu_2(\mu_3\text{-}CN)_2]$ motif in the structure of **2** and **8**. The formation of fused polygon rings, which form interwoven 2D-layers close packed by H-bonds, π–π stacking and Cu···Cu interaction, can be considered as a general feature in the structure of these SCP. **1** and **2** are luminescent materials which can be used in applications as
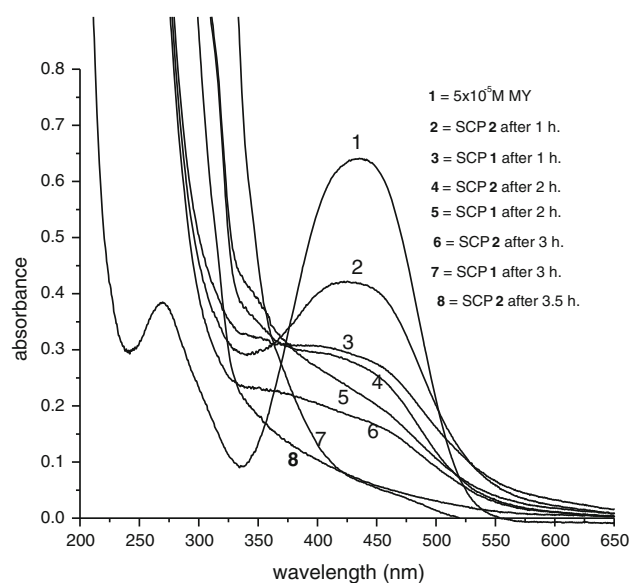
Fig. 6 The effect of time on the catalytic degradation of 5×10^{-5} M MY dye in the presence of H_2O_2 in absence and presence of the SCP **1** or **2**

Fig. 7 The IR spectra of the SCP **1** and **2** after the degradation process
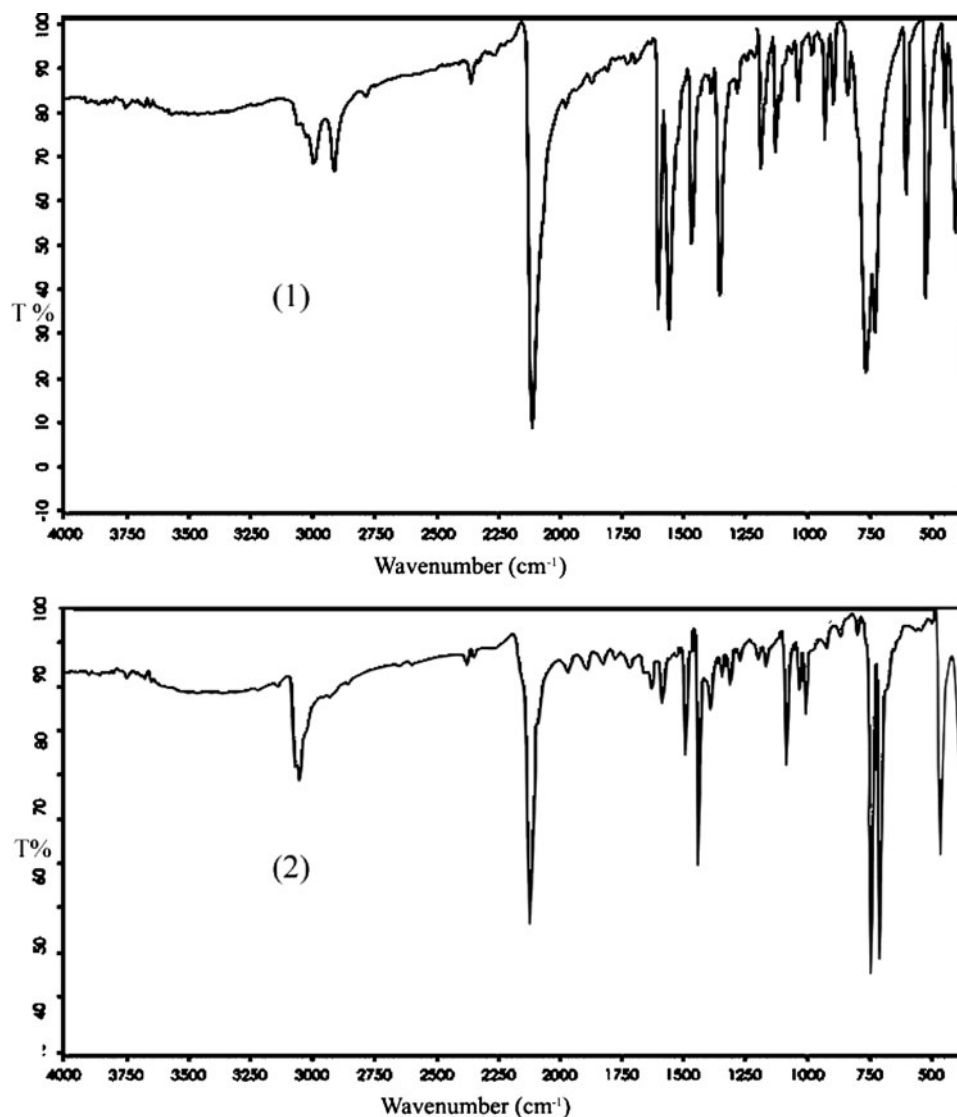
molecular sensing systems. Also, they can be used as catalysts towards the oxidation degradation of the MY dye.

5 Supplementary Data

CCDC 807066 contains the supplementary crystallographic data for **1**. These data can be obtained free of charge via http://www.ccdc.cam.ac.uk/conts/retrieving.html, or from the Cambridge Crystallographic Data Centre, 12 Union Road, Cambridge CB2 1EZ, UK; fax: (+44) 1223-336-033; or e-mail: deposit@ccdc.cam.ac.uk.

References

1. X. Lin, J. Jia, X. Zhao, K.M. Thomas, A.J. Blake, G.S. Ealker, N.R. Champness, P. Hubberstey, M. Schröder, Angew. Chem. Int. Ed. **45**, 7358 (2006)
2. Y.E. Cheon, M.P. Suh, Chem. Eur. J. **14**, 3961 (2008)
3. A. Brizard, M. Stuart, K.V. Bommel, A. Friggeri, M.D. Jong, J.V. Esch, Angew. Chem. Int. Ed. **47**, 2063 (2008)
4. C.B. Aakeröy, N.R. Champness, C. Janiak, Cryst. Eng. Commun. **12**, 22 (2010)
5. J.R. Li, R.J. Kuppler, H.C. Zhou, Chem. Soc. Rev. **38**, 1477 (2009)
6. A.U. Czaja, N. Trakhan, U. Müller, Chem. Soc. Rev. **38**, 1284 (2009)
7. Q.W. Li, W.Y. Zhang, O.S. Miljanic, C.H. Sue, Y.L. Zhao, L.H. Liu, C.B. Knobler, J.F. Stoddart, O.M. Yaghi, Science **325**, 855 (2009)
8. M.H. Alkordi, Y. Liu, R.W. Larson, J.F. Eubank, M. Eddaoudi, J. Am. Chem. Soc. **130**, 12639 (2008)
9. W.J. Rieter, K.M. Pott, K.M.L. Taylor, W.B. Lin, J. Am. Chem. Soc. **130**, 11584 (2008)
10. S.E.H. Etaiw, S.A. Amer, M.M. El-bendary, Polyhedron **28**, 2385 (2009)
11. S.E.H. Etaiw, S.A. Amer, M.M. El-bendary, J. Mater. Sci. **45**, 1307 (2010)
12. S.E.H. Etaiw, D.M. Abd El-Aziz, A.S. Badr El-din, Polyhedron **28**, 873 (2009)

13. S.E.H. Etaiw, A.S. Badr El-din, J. Inorg. Organomet. Polym. **20**, 684 (2010)
14. A.M.A. Ibrahim, E. Siebel, R.D. Fischer, Inorg. Chem. **37**, 3521 (1998)
15. E. Siebel, A.M.A. Ibrahim, R.D. Fischer, Inorg. Chem. **38**, 2530 (1999)
16. H. Hanika-Heidl, S.E.H. Etaiw, M.Sh. Ibrahim, A.S. Badr El-din, R.D. Fischer, J. Organomet. Chem. **684**, 329 (2003)
17. A.K. Brimah, E. Siebel, R.D. Fischer, N.A. Davies, D.C. Apperley, R.K. Harris, J. Organomet. Chem. **475**, 85 (1994)
18. S.E.H. Etaiw, S.N. Abdou, J. Inorg. Organomet. Polym. **20**, 622 (2010)
19. S.E.H. Etaiw, T.A. Fayed, M.B. El-Zaria, S.N. Abdou, J. Inorg. Organomet. Polym. **21**, 36 (2011)
20. S.E.H. Etaiw, T.A. Fayed, S.N. Abdou, J. Organomet. Chem. **695**, 1918 (2010)
21. S.E.H. Etaiw, M.E. El-Zaria, T.A. Fayed, S.N. Abdou, J. Inorg. Organomet. Polym. **21**, 465 (2011)
22. J.W. Eastes, W.M. Burgess, J. Am. Chem. **64**, 1187 (1942)
23. D.J. Chesnut, D. Plewak, J. Zubieta, J. Chem. Soc. Dalton Trans. 2567 (2001)
24. Y. Xu, Z.-G. Ren, H.-X. Li, W.-H. Zhang, J.-X. Chen, Y. Zhang, J.-P. Lang, J. Mol. Struct. **782**, 150–156 (2006)
25. J.H. Yu, J.Q. Xu, Q.X. Yang, L.Y. Pan, T.G. Wang, C.H. Lü, T.H. Ma, J. Mol. Struct. **658**, 1 (2003)
26. D. J. Chesnut, J. Zubieta, Chem. Commun. 1707 (1998)
27. D.J. Chesnut, A. Kusnetzow, R.R. Brige, J. Zubieta, Inorg. Chem. **38**, 5484 (1999)
28. T.A. Tronic, K.E. deKrafft, M.J. Lim, A.N. Ley, R.D. Pike, Inorg. Chem. **46**, 8897–8912 (2007)
29. S.-W. Liang, M.-X. Li, M. Shao, X. He, J. Mol. Struct. **875**, 17–21 (2008)
30. F.B. Stocker, M.A. Troester, D. Britton, J. Chem. Crystallogr. **30**, 389 (2000)
31. D.J. Chesnut, A. Kusnetzow, R.R. Birge, J. Zubieta, J. Chem. Soc. Dalton Trans. 2581 (2001)
32. X. He, C.-Z. Lu, C.-D. Wu, L.-J. Chen, Eur. J. Inorg. Chem. 2491 (2006)
33. T. Pretsch, J. Ostmann, C. Donner, M. Nahorska, J. Mroziński, H. Hartl, Inorg. Chim. Acta **358**, 2558–2564 (2005)
34. E. Colacio, J.M. Domínguez-Vera, F. Lloret, J.M. Moreno Sánchez, R. Kivekäs, A. Rodríguez, R. Sillanpää, Inorg. Chem. **42**, 4209–4214 (2003)
35. O. Teichert, W.S. Sheldrick, Z. Anorg, Allg. Chem. **626**, 1509 (2000)
36. X. He, C.-Z. Lu, D.-Q. Yuan, S.-M. Chen, J.-T. Chen, Eur. J. Inorg. Chem. 2181 (2005)
37. E.-M. Poll, S. Samba, R.D. Fischer, F. Olbrich, N.A. Davies, P. Avalle, D.C. Apperley, R.K. Harris, J. Solid, J. Solid State Chem. **152**, 286–301 (2000)
38. P. Avalle, R.K. Harris, H. Hanika-Heidl, R.D. Fischer, Solid State Sci. **6**, 1069–1076 (2004)
39. E.M. Poll, J.U. Schütze, R.D. Fischer, N.A. Davies, D.C. Apperley, R.K. Harris, J. Organomet. Chem. **621**, 254–260 (2001)
40. A.H. Pohl, A.M. Chippindale, S.J. Hibble, Solid State Sci. **8**, 379–387 (2006)
41. B. Liu, L. Xu, G.-C. Guo, J.-S. Huang, Inorg. Chem. Commun. **8**, 796–799 (2005)
42. X. Liu, G.-C. Guo, A.-Q. Wu, L.-Z. Cai, J.-S. Huang, Inorg. Chem. **44**, 4282–4286 (2005)
43. D.J. Chesnut, A. Kusnetzow, J. Zubieta, J. Chem. Soc. Dalton Trans. 4081 (1998)
44. R. Robson, B.F. Abrahams, S.R. Batten, R.W. Gable, B.F. Hoskins, J. Liu, in *Supramolecular Architecture*, ACS Symp. Ser. 499, ed. T. Bein (ACS, Washington, DC, 1992), p. 256 and refs. therein
45. T. Kitazawa, S.I. Nishikiori, Y. Yamagishi, R. Kuroda, T. Iwamoto, J. Chem. Soc. Chem. Commun. 413 (1992) and refs. therein
46. R. Eckhardt, R.D. Fischer, Inorg. Chem. Commun. **3**, 433–435 (2000)
47. A.M.A. Ibrahim, J. Organomet. Chem. **556**, 1–9 (1998)
48. L. Ronconi, C. Marazano, U. Russo, S. Sitran, R. Coraziani, D. Fregona, Appl. Organomet. Chem. **17**, 9 (2003)
49. S. Eller, P. Schwarz, A.K. Brimah, R.D. Fischer, D.C. Apperley, N.A. Davies, R.K. Harris, Organometallics **12**, 3232 (1993)
50. H.H. Jaffé, M. Orchin, *Theory and Applications of Ultraviolet Spectroscopy*, 5th printing (Wiley, New York, 1970)
51. S.E.H. Etaiw, M.M. El-bendary, J. Inorg. Organomet. Polym. **20**, 739 (2010) and references therein
52. A. Horváth, C.E. Wood, K.L. Stevenson, Inorg. Chem. **33**, 5351 (1994)
53. K.L. Stevenson, J.H. Jarboe, S.A. Langmeyer, T.W. Acra, Inorg. Chem. **42**, 3559 (2003)
54. K.D. Mantzavinos, E. Psillakis, J. Chem. Technol. Biotechnol. **79**, 431 (2004)
55. M. Neamtu, A. Yediler, I. Siminceaunu, A. Kettrup, J. Photochem. Photobiol. A **161**, 87 (2003)
56. T. Liu, H. You, O. Chen, J. Hazard. Mater. **162**, 860 (2009)
57. J.M. Monteagudo, A. Durán, I. San Martín, M. Aguirre, Appl. Catal. B **95**, 120 (2010)